doi:10.1038/nature11449

A single-atom electron spin qubit in silicon

Jarryd J. Pla[1], Kuan Y. Tan[1]†, Juan P. Dehollain[1], Wee H. Lim[1], John J. L. Morton[2]†, David N. Jamieson[3], Andrew S. Dzurak[1] & Andrea Morello[1]

A single atom is the prototypical quantum system, and a natural candidate for a quantum bit, or qubit—the elementary unit of a quantum computer. Atoms have been successfully used to store and process quantum information in electromagnetic traps[1], as well as in diamond through the use of the nitrogen–vacancy-centre point defect[2]. Solid-state electrical devices possess great potential to scale up such demonstrations from few-qubit control to larger-scale quantum processors. Coherent control of spin qubits has been achieved in lithographically defined double quantum dots in both GaAs (refs 3–5) and Si (ref. 6). However, it is a formidable challenge to combine the electrical measurement capabilities of engineered nanostructures with the benefits inherent in atomic spin qubits. Here we demonstrate the coherent manipulation of an individual electron spin qubit bound to a phosphorus donor atom in natural silicon, measured electrically via single-shot read-out[7–9]. We use electron spin resonance to drive Rabi oscillations, and a Hahn echo pulse sequence reveals a spin coherence time exceeding 200 μs. This time should be even longer in isotopically enriched ^{28}Si samples[10,11]. Combined with a device architecture[12] that is compatible with modern integrated circuit technology, the electron spin of a single phosphorus atom in silicon should be an excellent platform on which to build a scalable quantum computer.

There have been a number of proposals for the implementation of a spin-based qubit in silicon[13], though none have been studied in as much detail as the phosphorus atom qubit[14]. This interest has been motivated by the knowledge, developed over half a century from electron spin resonance experiments on bulk-doped phosphorus in silicon[15], that spin coherence times can be exceptionally long, exceeding seconds[11]. This is due to the availability of silicon in an enriched nuclear spin-zero (^{28}Si) form, as well as the low spin-orbit coupling in silicon[15]. The use of donor electron spins has further advantages of consistency (because each atom is identical) and tuneability (for example, through the Stark shift[16]), and the donor atom's nuclear spin can be employed as a quantum memory for longer term storage[17].

Using methods compatible with existing complementary metal-oxide-semiconductor (CMOS) technology, we fabricated a nanostructure device on the SiO_2 surface to enable read-out and control of an electron spin[12] (Fig. 1a). In this work, the donor is intentionally implanted into the silicon substrate, with future options including the use of deterministic ion implantation[18] or atomic precision in donor placement through scanning probe lithography[19]. The device is placed in a magnetic field of approximately 1 T, yielding well-defined electron spin-down and spin-up states ($|\downarrow\rangle$ and $|\uparrow\rangle$).

Transitions between the electron $|\downarrow\rangle$ and $|\uparrow\rangle$ states are driven by an oscillating magnetic field generated by applying microwaves to an on-chip broadband transmission line[4,20]. By operating at a high magnetic field and low temperature ($T_{\mathrm{electron}} \approx 300$ mK), we can detect these transitions through single-shot projective measurements on the electron spin with a process known as spin-to-charge conversion[7,8]. Here the donor electron is both electrostatically coupled and tunnel-coupled to the island of a single electron transistor (SET), with the SET serving as both a sensitive charge detector and an electron reservoir for the donor. Using gates PL and TG (Fig. 1a) to tune the electrochemical potentials of the donor electron spin states ($\mu_\downarrow$ and $\mu_\uparrow$ for states $|\downarrow\rangle$ and $|\uparrow\rangle$) and the Fermi level in the SET island (μ_{SET}), we can discriminate between a $|\downarrow\rangle$ or $|\uparrow\rangle$ electron as well as perform electrical initialization of the qubit, following the procedure introduced in ref. 8.

Our experiments use a two-step cyclical sequence of the donor potential, alternating between a spin read-out/initialization phase and a coherent control phase (see Supplementary Video). The qubit is first initialized in the $|\downarrow\rangle$ state through spin-dependent loading by satisfying the condition $\mu_\downarrow < \mu_{\mathrm{SET}} < \mu_\uparrow$ (Fig. 1b). After this, the system is brought into a regime where the spin is a stable qubit ($\mu_\downarrow, \mu_\uparrow \ll \mu_{\mathrm{SET}}$) and manipulated with various microwave pulse schemes resonant with the spin transition (Fig. 1c). The spin is then read out electrically via spin-to-charge conversion (Fig. 1b), a process which produces a pulse in the current through the SET (that is, I_{SET}) if the electron was $|\uparrow\rangle$, and leaves the qubit initialized $|\downarrow\rangle$ for the next cycle.

The electron spin resonance frequency can be extracted from the spin Hamiltonian describing this system (see also Fig. 1d):

$$H = \gamma_e B_0 S_z - \gamma_n B_0 I_z + A S\cdot I \qquad (1)$$

where γ_e (or γ_n) is the gyromagnetic ratio of the electron (or nucleus), B_0 is the externally applied magnetic field, S (or I) is the electron (or nuclear) spin operator with z-component S_z (or I_z) and A is the hyperfine constant. If $\gamma_e B_0 \gg A$, the states shown in Fig. 1d are good approximations for the eigenstates of equation (1). Allowed transitions involving flips of the electron spin only (identified by arrows in Fig. 1d) exhibit resonance frequencies that depend on the state of the ^{31}P nuclear spin: $\nu_{e1} \approx \gamma_e B_0 - A/2$ for nuclear spin-down; and $\nu_{e2} \approx \gamma_e B_0 + A/2$ for nuclear spin-up. The transition frequencies ν_{e1} and ν_{e2} are found by conducting an electron spin resonance (ESR) experiment[21], which is described in the Supplementary Information.

To demonstrate coherent control, we apply a single microwave pulse of varying duration t_p to perform Rabi oscillations of the electron spin. For each t_p the cyclic pulse sequence (Fig. 1e, f) is repeated 20,000 times, first with a microwave frequency ν_{e1}, and immediately after at ν_{e2}. It is necessary to pulse on both ESR transitions as the ^{31}P nuclear spin can flip several times during acquisition of the data in Fig. 2a. Figure 1g displays single-shot traces of the SET output current I_{SET} for four consecutive repetitions of the measurement sequence, for an arbitrary pulse length. A threshold detection method[8] is used to determine the fraction of shots that contain a $|\uparrow\rangle$ electron for the measurements at both frequencies. Figure 2a shows the electron spin-up fraction $f_\uparrow$ as a function of the microwave pulse duration for different applied powers P_{ESR}. The fits through the data are derived from simulations assuming Gaussian fluctuations of the local field (see Supplementary Information). Confirmation that these are Rabi oscillations comes from the linear dependence of the Rabi frequency with the applied microwave amplitude ($P_{\mathrm{ESR}}^{1/2}$), that is, $f_{\mathrm{Rabi}} = \gamma_e B_1$. Here B_1 is taken as half of the total linear oscillating magnetic field amplitude generated by the transmission line at the site of the donor,

[1]Centre for Quantum Computation and Communication Technology, School of Electrical Engineering & Telecommunications, University of New South Wales, Sydney, New South Wales 2052, Australia. [2]Department of Materials, Oxford University, Oxford OX1 3PH, UK. [3]Centre for Quantum Computation and Communication Technology, School of Physics, University of Melbourne, Melbourne, Victoria 3010, Australia. †Present addresses: Department of Applied Physics/COMP, Aalto University, PO Box 13500, FI-00076 Aalto, Finland (K.Y.T.); London Centre for Nanotechnology, University College London, London WC1H 0AH, UK (J.J.L.M.).

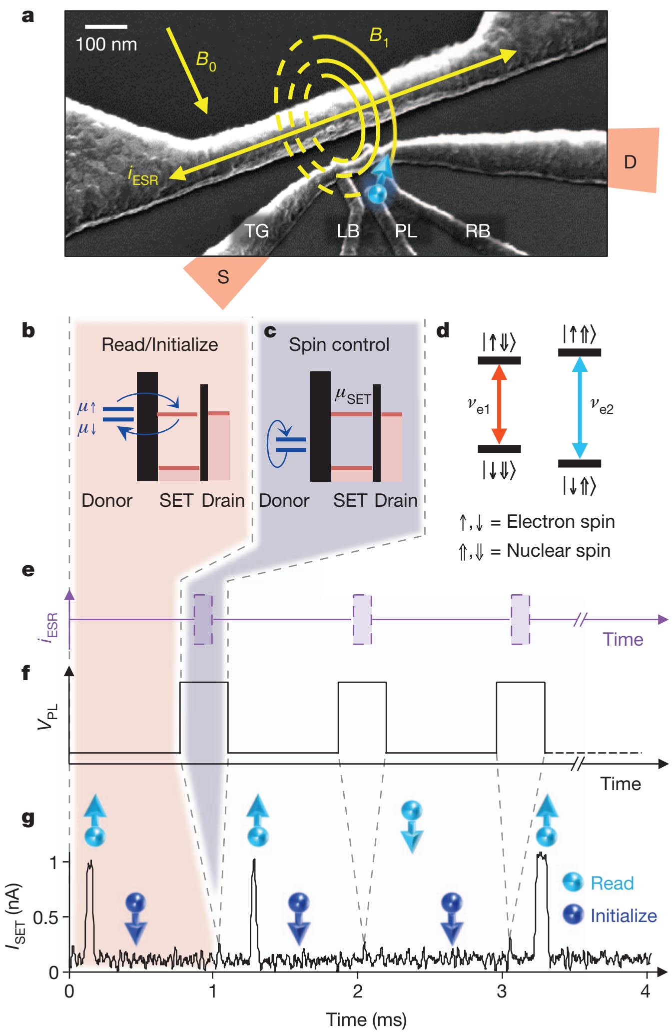

Figure 1 | Qubit device and pulsing scheme. **a**, Scanning electron micrograph of a qubit device similar to the one used in the experiment. The SET (lower right portion) consists of a top gate (TG), plunger gate (PL), left and right barrier gates (LB and RB) and source/drain contacts (S and D). The microwave transmission line is shown in the upper left portion. The donor (blue) is subject to an oscillating magnetic field B_1 from the transmission line which is perpendicular to the in-plane external field B_0. **b** and **c**, Pulse sequence for the qubit initialization, control and read-out. **b**, Read/initialization phase $\mu_\downarrow < \mu_{\mathrm{SET}} < \mu_\uparrow$: a spin-up electron will tunnel from the donor to the SET island, to be later replaced by a spin-down electron, causing a pulse of current through the SET. A spin-down electron remains trapped on the donor throughout the entire phase. **c**, Control phase $\mu_\downarrow, \mu_\uparrow \ll \mu_{\mathrm{SET}}$: electron spin states are plunged well below the SET island Fermi level while microwaves are applied to the transmission line to perform electron spin resonance. **d**, Energy level diagram of the ^{31}P electron-nuclear system. **e** and **f**, Microwave pulse sequence (**e**) and synchronized PL gate voltage waveform (**f**) for performing and detecting spin manipulations (not drawn to scale). An arbitrary ESR pulse sequence is represented by each of the dashed purple boxes in panel **e**. **g**, Example of I_{SET} response to four consecutive read/control events where a single microwave pulse of duration t_p is applied, taken at $B_0 = 1.07$ T. The pulse duration t_p has been set to give a high probability of flipping the electron spin. The duration of the pulses in I_{SET} gives the electron spin-down tunnel-in time (about 33 μs), while their delay from the beginning of the read phase gives the spin-up tunnel-out time (about 295 μs).

assuming the rotating-wave approximation. Figure 2b shows the expected linear behaviour with microwave amplitude of the Rabi frequencies extracted from the data in Fig. 2a. The largest Rabi frequency attained was 3.3 MHz ($B_1 \approx 0.12$ mT), corresponding to a $\pi/2$ rotation in about 75 ns.

The qubit manipulation time should be contrasted with the coherence lifetime of the qubit, termed T_2. Possible sources of decoherence include spectral diffusion of the ^{29}Si bath spins[15,22,23], noise in the external magnetic field, and paramagnetic defects and charge traps at the Si/SiO$_2$ interface[24]. These mechanisms can, to a degree, be compensated for by using spin echo techniques (Fig. 3a), as long as the fluctuations are slow compared with the electron spin manipulation time (typically around 100 ns).

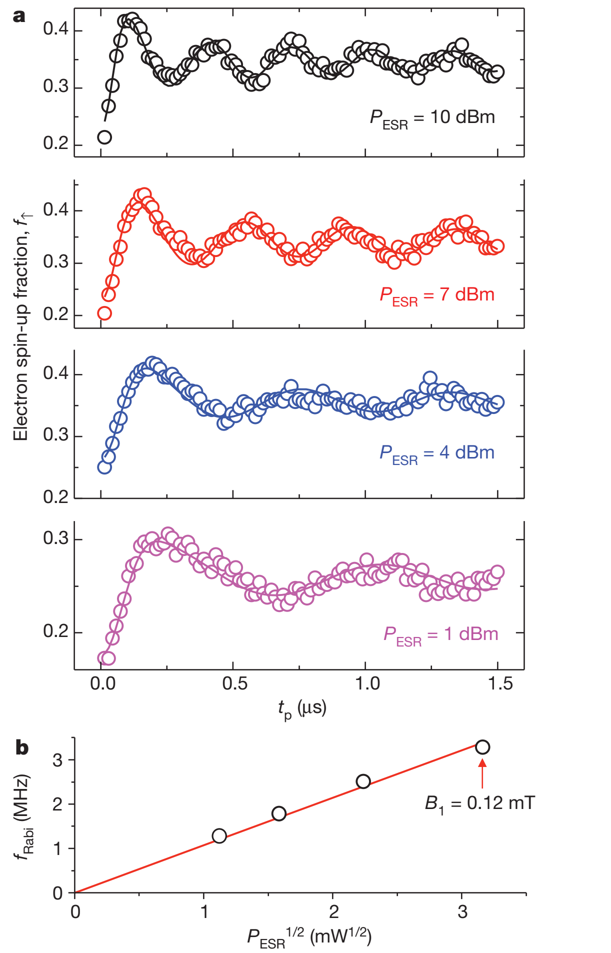

Figure 2 | Rabi oscillations and power dependence of the Rabi frequency. **a**, Electron spin-up fraction as a function of the microwave burst duration for varying input powers P_{ESR}. Measurements were performed at an external field of $B_0 = 1.07$ T where the ESR frequencies are $\nu_{e1} = 29.886$ GHz and $\nu_{e2} = 30.000$ GHz. Each point represents an average of 20,000 single-shot measurements, with each shot about 1 ms in duration (see Supplementary Information for further details). The solid lines are fits generated from simulations of the measurements (Supplementary Information). **b**, Rabi frequency versus the microwave excitation amplitude, with a fit displaying the linear relationship.

Figure 3a presents the gate voltage and microwave pulsing scheme for a Hahn echo measurement. Dephasing resulting from static local contributions to the total effective field during an initial period τ_1 is (partially or fully) refocused by a π rotation followed by a second period τ_2 (see Fig. 3c for a Bloch sphere state evolution). A spin echo is observed by varying the delay τ_2 and recording the spin-up fraction. In Fig. 3e we plot the difference in delay times $(\tau_2 - \tau_1)$ against $f_\uparrow$. For $\tau_1 = \tau_2$, we expect to recover a $|\downarrow\rangle$ electron at the end of the sequence if little dephasing occurs (that is, for short τ), and hence observe a minimum in $f_\uparrow$. When $\tau_2 - \tau_1 \neq 0$, imperfect refocusing results in an increase in the recovered spin-up fraction. The echo shape is approximated as being Gaussian and the half-width at half-maximum implies a pure dephasing time of $T_2^* = 55 \pm 5$ ns.

We now set $\tau = \tau_1 = \tau_2$ and monitor the spin-up fraction as a function of τ, to obtain the spin echo decay curve of Fig. 3f. A fit of the form

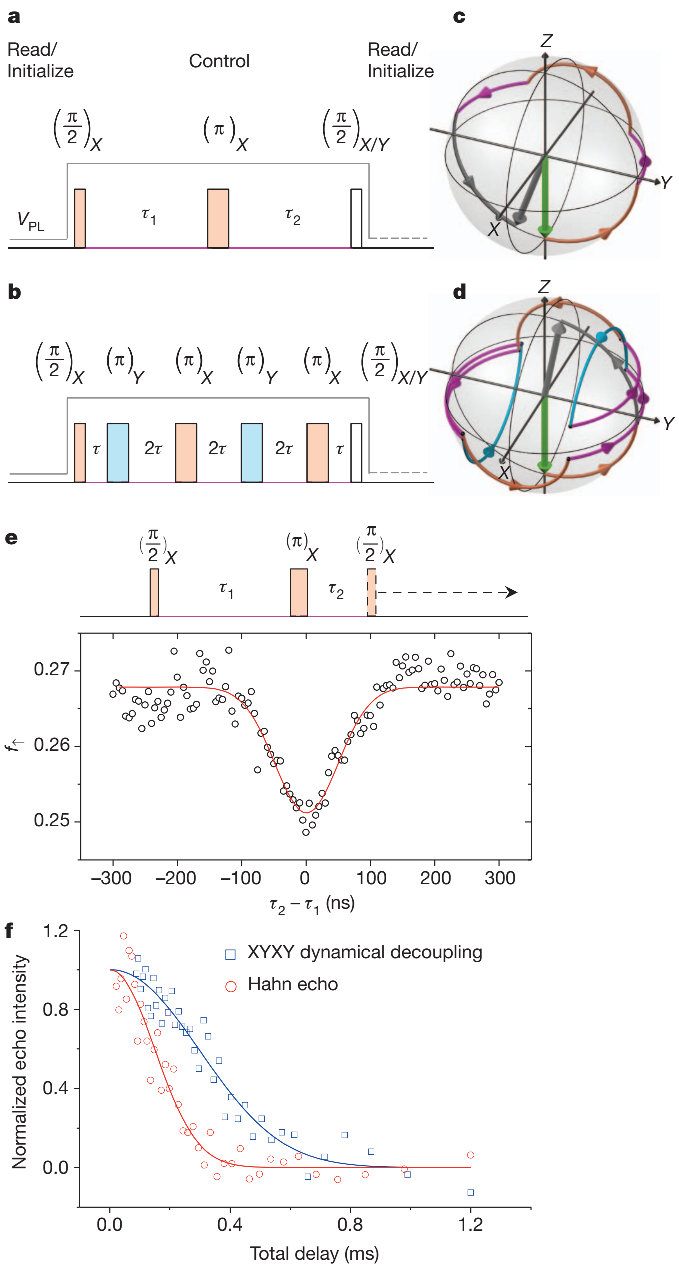

Figure 3 | Coherence time and dynamical decoupling. **a** and **b**, Pulse protocols for the Hahn echo (**a**) and *XYXY* dynamical decoupling (**b**) sequences with accompanying PL gate voltage waveforms, as described in the main text. The rotation angles are displayed above each pulse in brackets, with the subscript (*X* or *Y*) denoting the axis on the Bloch sphere about which the rotation is applied. The read/initialization time is 1 ms. All measurements were performed at $B_0 = 1.07$ T and with $P_{ESR} = 10$ dBm, where a $\pi/2$ rotation takes around 75 ns. **c** and **d**, Bloch sphere representation of the evolution in the rotating frame for the Hahn echo (**c**) and *XYXY* (**d**) sequences. The green arrow represents the initial spin state $|\downarrow\rangle$, while the grey arrow represents the final state for the case when the second $\pi/2$ pulse is about *X* (*Y* is not shown). The purple path represents dephasing in between pulses, the orange path represents a rotation about *X*, and the blue path is a rotation about *Y*. We have included rotation angle errors of 5° and 15° for the $\pi/2$ and π pulses respectively. **e**, An echo curve, obtained by applying the depicted pulse sequence with a fixed τ_1 (=10 μs) and varying τ_2. Each point represents the electron spin-up fraction $f_\uparrow$ calculated from 50,000 single shots acquired at both ESR frequencies ($\nu_{e1} = 29.886$ GHz and $\nu_{e2} = 30.000$ GHz) and summed. The fit in red is Gaussian and of the form $f_\uparrow = B\exp(-[(\tau_2-\tau_1)/C]^2) + D$. **f**, Hahn echo (or *XYXY* dynamical decoupling) decay in red circles (or blue squares), measured via simulated quadrature detection (see the Methods for details). A fit through the data is given by $y = \exp[(-(N\tau/T_2)^b]$, where $N = 2$ (or $N = 8$) for the Hahn echo (or *XYXY* dynamical decoupling) experiment. Parameter values are discussed in the main text.

$y = \exp(-(2\tau/T_2)^b)$, where T_2 and b are free parameters, yields $T_2 = 206 \pm 12$ μs and $b = 2.1 \pm 0.4$. The coherence time T_2 is almost a factor of 2,000 times longer than T_2*, and is remarkably close to the value (300 μs) measured in bulk-doped natural silicon samples[25]. Variations in T_2 can be expected, depending on the exact distribution of ^{29}Si nuclei within the extent of the donor electron wavefunction. This indicates that the presence of a nearby SET and the close proximity of the Si/SiO_2 interface have little, if any, effect on the electron spin coherence. This is not entirely surprising, because paramagnetic centres at the Si/SiO_2 interface are expected to be fully spin-polarized under our experimental conditions $g\mu_B B_0 \gg k_B T$ (where g is the donor electron Landé g-factor, μ_B is the Bohr magneton and k_B is the Boltzmann constant), leading to an exponential suppression of their spin fluctuations[26]. Direct flip-flop transitions between the donor qubit and nearby interface traps are suppressed by the difference in g-factor ($g = 1.9985$ for the donor, $g > 2$ for the traps[21]), whereas dipolar flip-flops with nearby donors[27] can appear as a T_1 process[8] on a much longer timescale. We measured $T_1 \approx 0.7$ s at $B_0 = 2.5$ T (data not shown), implying that this process has no bearing on T_2. The echo decay is Gaussian in shape ($b = 2.1 \pm 0.4$), consistent with decoherence dominated by ^{29}Si spectral diffusion[22].

We have extended the coherence time by applying an *XYXY* dynamical decoupling ESR pulse sequence[28] (Fig. 3b and d). This sequence substitutes the single π rotation of the Hahn echo with a series of four π rotations alternating about the X and Y axes, achieved by applying adjacent π pulses that are 90° out of phase. The resulting echo decay is shown in Fig. 3f, with a fit to the data yielding $T_2 = 410 \pm 20$ μs and $b = 2.1 \pm 0.4$. As well as representing a factor-of-two improvement in T_2, the *XYXY* sequence demonstrates the ability to perform controlled rotations about two orthogonal axes on the Bloch sphere (X and Y), permitting arbitrary one-qubit gates for universal quantum computing[29].

Next we consider the fidelity of our electron spin qubit, broken down into three components: measurement, initialization and control. The measurement fidelity F_M comprises errors resulting from detection limitations of the experimental set-up as well as thermally induced read-out events. The electrical spin-down and spin-up read errors ($\gamma_\downarrow$ and $\gamma_\uparrow$ respectively) arise from a finite measurement bandwidth and signal-to-noise ratio. They depend on the threshold current I_T used for detecting the spin-up pulses. Figure 4a shows the results of a numerical model based on our experimental data (see Supplementary Information for details), where $\gamma_{\downarrow,\uparrow}$ are plotted as a function of I_T. At $I_T = 370$ pA we achieve a best-case error of $\gamma = \gamma_\downarrow + \gamma_\uparrow = 18\%$.

Thermal broadening of the Fermi distribution in the SET island produces the read/load errors, as depicted in Fig. 4b. The process of a spin-down electron tunnelling into an empty state in the SET occurs with a probability α, whereas β denotes the probability of incorrectly initializing the qubit in the spin-up state. The parameters α and β are sensitive to the device tuning and can vary slightly between measurements. We have extracted α and β from simulations of the Rabi oscillations in Fig. 2a, and for $P_{ESR} = 10$ dBm we find $\alpha = 28 \pm 1\%$ and $\beta = 1^{+9}_{-1}\%$. This gives an average measurement fidelity for the electron spin-up and spin-down states of $F_M = 1 - (\gamma + \alpha(1-\gamma_\downarrow))/2 = 77 \pm 2\%$ and an initialization fidelity F_I of at least 90% (see Supplementary Information for full details).

The qubit control fidelity F_C is reduced by random field fluctuations from the ^{29}Si nuclear bath spins. These produce an effective field B_{eff} in the rotating frame that is tilted out of the X–Y plane (Fig. 4d), and lead to imperfect pulses. We now estimate the strength of these fluctuations. Figure 4c presents a series of ESR spectra, where the electron spin-up fraction is monitored as a function of the microwave frequency. The top three traces of Fig. 4c contain individual sweeps with each point obtained over a timescale of around 250 ms. We attribute the shift in peak position between sweeps to slow fluctuations of a few strongly coupled ^{29}Si nuclei, with hyperfine coupling strengths of the order of 1 MHz. The width of the peaks is most probably the result of

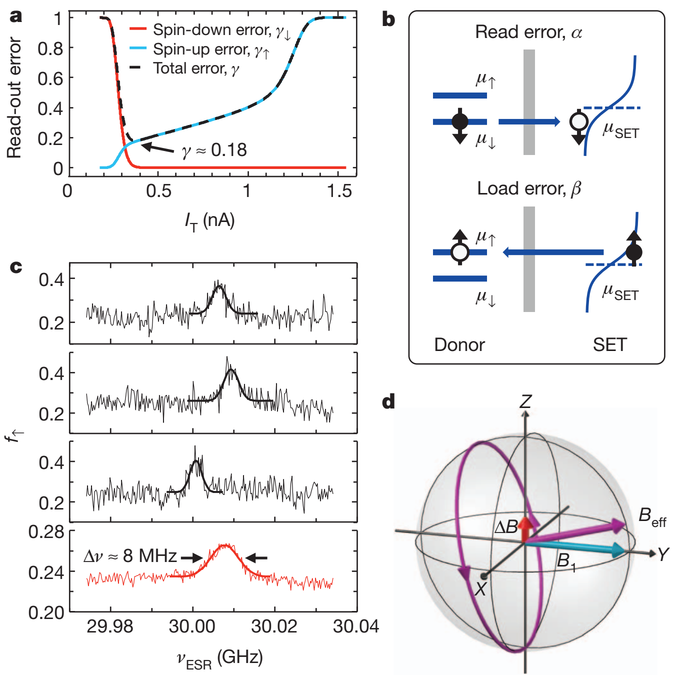

Figure 4 | Qubit fidelity analysis. a, Electrical read-out errors generated from a numerical model. The red curve gives the error $\gamma_\downarrow$ involved in identifying a $|\downarrow\rangle$ electron as a function of the threshold current I_T, caused by noise in I_{SET} exceeding I_T. The blue curve represents the error $\gamma_\uparrow$ for detecting a $|\uparrow\rangle$ electron, which occurs as a result of detection bandwidth limitations and a finite $|\uparrow\rangle$ I_{SET} pulse height[8]. The dashed curve depicts the combined electrical error, $\gamma = \gamma_\downarrow + \gamma_\uparrow$. **b**, Mechanisms by which read (top) and load (bottom) errors are produced as a result of thermal broadening in the SET island (discussed in the main text). The solid circles represent full electron states with spin indicated by the arrow, while the empty circles signify unoccupied states. **c**, Sweeps of the frequency ν_{ESR} in the vicinity of the nuclear spin-up ESR transition ν_{e2}. The top three traces are individual sweeps where $f_\uparrow$ at each ν_{ESR} is calculated from 250 single-shot measurements. The bottom trace is an average of 100 sweeps. **d**, Illustration of the rotation errors created by hyperfine field fluctuations of the ^{29}Si nuclear bath. For simplicity, only the Z-component of the hyperfine field has been shown. The bath nuclear spins produce an offset from resonance, ΔB, which causes rotations about a new axis aligned with B_{eff}.

distant, weakly coupled ^{29}Si nuclear spins that fluctuate on the single-shot timescale (see Supplementary Information for further discussion). The bottom trace of Fig. 4c contains an average of 100 sweeps, representing many nuclear spin configurations. From this we extract a full-width at half-maximum $\Delta\nu = 7.5 \pm 0.5$ MHz. This is consistent with the observed T_2*, where $\Delta\nu = 1/(\pi T_2{}^*) = 6 \pm 1$ MHz. To calculate the rotation angle error, we simulate a Rabi experiment assuming the largest B_1 achieved (0.12 mT) and Gaussian fluctuations of the nuclear bath with a standard deviation of $\sigma = \Delta\nu/\left(2\sqrt{2\ln(2)}\right) = 3.2 \pm 0.2$ MHz (see Supplementary Information). From this we infer an average tip angle of $102 \pm 3^\circ$ for an intended π rotation, corresponding to an average control fidelity of $F_C = 57 \pm 2\%$.

The processes that contribute to the measurement, initialization and control fidelity degradation can be mitigated with foreseeable adjustments to the device architecture and experimental set-up. Significant improvements in the read/load errors would follow from enhanced electrical filtering to lower the electron temperature, thus enabling the high read-out fidelities (>90%) already achieved[8]. Moving to an enriched ^{28}Si (nuclear spin-zero) substrate[10] would remove the primary source of rotation angle error, and allow for the exceptional coherence times already demonstrated in bulk-doped samples[11].

Future experiments will focus on the coupling of two donor electron spin qubits through the exchange interaction[14], a key requirement in proposals for scalable quantum computing architectures in this system[30]. Taken together with the single-atom doping technologies[18,19] now demonstrated in silicon, the advances reported here open the way for a spin-based quantum computer using single atoms, as first envisaged by Kane[14] more than a decade ago.

METHODS SUMMARY

Device fabrication and experimental set-up. For information relating to the device fabrication and experimental set-up, see the Supplementary Information.

Simulated quadrature detection for T_2 measurements. For each τ ($\tau = \tau_1 = \tau_2$ for the Hahn echo), the sequence of Fig. 3a (or Fig. 3b) is repeated 30,000 times (or 75,000 times) for the Hahn echo (or $XYXY$ dynamical decoupling) measurement at both ν_{e1} and ν_{e2}, and for X and Y phases of the final $\pi/2$ rotation. The resulting signal amplitude is given by $(f_\uparrow(\nu_{e1}, Y) - f_\uparrow(\nu_{e1}, X)) + (f_\uparrow(\nu_{e2}, Y) - f_\uparrow(\nu_{e2}, X))$, where $f_\uparrow(\nu_{e1}, Y)$ represents the electron spin-up fraction of the single-shot traces taken at ν_{e1} with a final $\pi/2$ pulse about the Y-axis, and so on. The data points in Fig. 3f have been re-normalized with the amplitudes and offsets extracted from free-exponent fits through the decays. A 30% reduction in signal amplitude was observed for the $XYXY$ dynamical decoupling decay, relative to that of the Hahn echo.

Received 16 May; accepted 27 July 2012.
Published online 19 September 2012.

1. Biercuk, M. J. *et al.* Optimized dynamical decoupling in a model quantum memory. *Nature* **458,** 996–1000 (2009).
2. van der Sar, T. *et al.* Decoherence-protected quantum gates for a hybrid solid-state spin register. *Nature* **484,** 82–86 (2012).
3. Petta, J. R. *et al.* Coherent manipulation of coupled electron spins in semiconductor quantum dots. *Science* **309,** 2180–2184 (2005).
4. Koppens, F. H. L. *et al.* Driven coherent oscillations of a single electron spin in a quantum dot. *Nature* **442,** 766–771 (2006).
5. Nowack, K. C., Koppens, F. H. L., Nazarov, Y. V. & Vandersypen, L. M. K. Coherent control of a single electron spin with electric fields. *Science* **318,** 1430–1433 (2007).
6. Maune, B. M. *et al.* Coherent singlet-triplet oscillations in a silicon-based double quantum dot. *Nature* **481,** 344–347 (2012).
7. Elzerman, J. M. *et al.* Single-shot read-out of an individual electron spin in a quantum dot. *Nature* **430,** 431–435 (2004).
8. Morello, A. *et al.* Single-shot readout of an electron spin in silicon. *Nature* **467,** 687–691 (2010).
9. Simmons, C. B. *et al.* Tunable spin loading and T_1 of a silicon spin qubit measured by single-shot readout. *Phys. Rev. Lett.* **106,** 156804 (2011).
10. Ager, J. W. *et al.* High-purity, isotopically enriched bulk silicon. *J. Electrochem. Soc.* **152,** G448–G451 (2005).
11. Tyryshkin, A. M. *et al.* Electron spin coherence exceeding seconds in high purity silicon. *Nature Mater.* **11,** 143–147 (2012).
12. Morello, A. *et al.* Architecture for high-sensitivity single-shot readout and control of the electron spin of individual donors in silicon. *Phys. Rev. B* **80,** 081307(R) (2009).
13. Morton, J. J. L., McCamey, D. R., Eriksson, M. A. & Lyon, S. A. Embracing the quantum limit in silicon computing. *Nature* **479,** 345–353 (2011).
14. Kane, B. E. A silicon-based nuclear spin quantum computer. *Nature* **393,** 133–137 (1998).
15. Feher, G. & Gere, E. A. Electron spin resonance experiments on donors in silicon. II. Electron spin relaxation effects. *Phys. Rev.* **114,** 1245–1256 (1959).
16. Bradbury, F. R. *et al.* Stark tuning of donor electron spins in silicon. *Phys. Rev. Lett.* **97,** 176404 (2006).
17. Morton, J. J. L. *et al.* Solid-state quantum memory using the 31P nuclear spin. *Nature* **455,** 1085–1088 (2008).
18. Jamieson, D. N. *et al.* Controlled shallow single-ion implantation in silicon using an active substrate for sub-20-keV ions. *Appl. Phys. Lett.* **86,** 202101 (2005).
19. Fuechsle, M. *et al.* A single-atom transistor. *Nature Nanotechnol.* **7,** 242–246 (2012).
20. Dehollain, J. P. *et al.* Nanoscale broadband transmission lines for spin qubit control. Preprint at http://arxiv.org/abs/1208.2421v1 (2012).
21. Xiao, M., Martin, I., Yablonovitch, E. & Jiang, H. W. Electrical detection of the spin resonance of a single electron in a silicon field-effect transistor. *Nature* **430,** 435–439 (2004).
22. Chiba, M. & Hirai, A. Electron spin echo decay behaviours of phosphorus doped silicon. *J. Phys. Soc. Jpn* **33,** 730–738 (1972).
23. Witzel, W. M. & Das Sarma, S. Quantum theory for electron spin decoherence induced by nuclear spin dynamics in semiconductor quantum computer architectures: Spectral diffusion of localized electron spins in the nuclear solid-state environment. *Phys. Rev. B* **74,** 035322 (2006).
24. Schenkel, T. *et al.* Electrical activation and electron spin coherence of ultralow dose antimony implants in silicon. *Appl. Phys. Lett.* **88,** 112101 (2006).
25. Tyryshkin, A. M. *et al.* Coherence of spin qubits in silicon. *J. Phys. Condens. Matter* **18,** S783–S794 (2006).
26. Morello, A., Stamp, P. C. E. & Tupitsyn, I. S. Pairwise decoherence in coupled spin qubit networks. *Phys. Rev. Lett.* **97,** 207206 (2006).
27. Witzel, W. M., Carroll, M. S., Morello, A., Cywiński, Ł. & Das Sarma, S. Electron spin decoherence in isotope-enriched silicon. *Phys. Rev. Lett.* **105,** 187602 (2010).
28. Tyryshkin, A. M. *et al.* Dynamical decoupling in the presence of realistic pulse errors. Preprint at http://arxiv.org/abs/1011.1903v2 (2010).
29. Barenco, A. *et al.* Elementary gates for quantum computation. *Phys. Rev. A* **52,** 3457–3467 (1995).

30. Hollenberg, L. C. L., Greentree, A. D., Fowler, A. G. & Wellard, C. J. Two-dimensional architectures for donor-based quantum computing. *Phys. Rev. B* **74,** 045311 (2006).

Supplementary Information is available in the online version of the paper.

Acknowledgements We thank R. P. Starrett, D. Barber, C. Y. Yang and R. Szymanski for technical assistance. We also thank A. Laucht for the Bloch sphere artwork and D. Reilly for comments on the manuscript. This research was funded by the Australian Research Council Centre of Excellence for Quantum Computation and Communication Technology (project number CE11E0096) and the US Army Research Office (W911NF-08-1-0527). We acknowledge support from the Australian National Fabrication Facility.

Author Contributions K.Y.T. and W.H.L. fabricated the device; D.N.J. designed the phosphorus implantation experiments; J.J.P., K.Y.T., J.J.L.M. and J.P.D. performed the measurements; J.J.P., A.M., A.S.D. and J.J.L.M. designed the experiments and discussed the results; J.J.P. analysed the data; J.J.P. wrote the manuscript with input from all co-authors.

Author Information Reprints and permissions information is available at www.nature.com/reprints. The authors declare no competing financial interests. Readers are welcome to comment on the online version of the paper. Correspondence and requests for materials should be addressed to J.J.P. (jarryd@unsw.edu.au) or A.M. (a.morello@unsw.edu.au).